



Article

Remote Radio-Physical Harbingers of Drought in Steppes of the South of Western Siberia

Andrey Romanov *, Ivan Ryabinin , Ilya Khvostov, Dmitry Troshkin and Dmitry Romanov

Institute for Water and Environmental Problems SB RAS, 1 Molodezhnaya St., Barnaul 656038, Russia

* Correspondence: romanov_alt@mail.ru; Tel.: +7-(385-2)-66-64-62

Abstract: Methods for remote sensing of the underlying surface in the microwave range based on moisture dependence of soil emissivity were successfully used in monitoring droughts and assessing water availability of the studied territories. Soil moisture influence on soil cover emissivity calibrated in units of the radio brightness temperature (T_B) was studied. We used values of T_B derived from SMOS satellite data. This paper presents the results of a comparative analysis of soil, meteorological conditions and physical characteristics of soils in the test territories of the Kulunda Plain. The experimental data were applied in computing trends of T_B and physical temperature (T) described by linear dependencies. Volume fractions of water (W) in soil were calculated based on the satellite sensing data, the results of field studies and laboratory measurements of dielectric characteristics of soils. A map scheme of spatial distribution of W was constructed and the influences of snow cover, precipitation and surface wind velocity on drought were analyzed. The comprehensive analysis of remote, field and laboratory data suggest that the rate of change in the brightness temperature (dT_{BH}/dT —up to 17 K per day), which characterizes the rate of fall in volume humidity of soil (ΔW —up to 0.009 cm³/cm³ per day), can be used as a short-term radio-physical harbinger of drought. An experimental dependence of the rate of change in radio brightness temperature on the rate of change in soil moisture was established.

Keywords: satellite; microwave sensing; drought; Western Siberia



Citation: Romanov, A.; Ryabinin, I.; Khvostov, I.; Troshkin, D.; Romanov, D. Remote Radio-Physical Harbingers of Drought in Steppes of the South of Western Siberia. *Remote Sens.* **2022**, *14*, 6141. <https://doi.org/10.3390/rs14236141>

Academic Editors: Tobias Landmann and Olena Dubovyk

Received: 19 October 2022

Accepted: 1 December 2022

Published: 3 December 2022

Publisher's Note: MDPI stays neutral with regard to jurisdictional claims in published maps and institutional affiliations.



Copyright: © 2022 by the authors. Licensee MDPI, Basel, Switzerland. This article is an open access article distributed under the terms and conditions of the Creative Commons Attribution (CC BY) license (<https://creativecommons.org/licenses/by/4.0/>).

1. Introduction

Arid lands, widespread all over the world, cover approximately 40% of the total land surface. Vital activity of billions of people often depends on droughts—dangerous natural events which occur with different frequency and intensity worldwide [1]. Prolonged droughts change the existing relationships between natural systems and cause territory desertification and soil/vegetation degradation. The combined effect of these negative processes contributes to a noticeable drop in crop yields that, in turn, increases costs of crop production and becomes a serious threat to national food security in many countries [2,3].

Droughts, which significantly reduce the volume of agricultural products throughout the world, contributed to the global food crisis of 2007–2008 and a sharp rise in food prices. The resolution of the crisis, which affected more than 850 million people, required urgent effective measures, including the promotion of sustainable farming methods in the context of climate change, the increased public investment in agriculture and the reform of global food aid institutions [4]. In 2021, between 702 and 828 million people suffered from famine [5].

In the last decade, the growing concerns over food security throughout the world and especially in developing countries attracted heightened interest in the problems of mitigating the negative effects of natural hazards (primarily droughts) and anthropogenic factors on the ecological state of agricultural lands. Much attention was also paid to the development of methods for assessing the impact of dominant agro-food systems on the environment [6]. Soil drought, which occurs with the drop in precipitation amount below

normal and the decrease in water availability of the territory, is characterized by the regional (often unique) features depending on meteorological conditions, climatic parameters, orography, type, particle-size composition and salinity of soil [7] and atmosphere circulation responsible for transfer of air masses [8].

To date, more than 170 drought indices have been developed, but none of them guarantee an accurate forecast of scale, timing, duration and intensity of droughts [9]. Moreover, the performance of drought indices (already repeatedly tested in different regions of the world) fails under changing climate conditions and increasing anthropogenic impacts on ecosystems [10–13]. The best methods for assessing droughts are based on the results of ground-based observations. In [10,14,15], a description of some drought indices widely used in recent years is given. The joint analysis of such indices makes it possible to choose a suitable drought index for a specific region.

In 2012, Northern Eurasia was in the grip of the strongest (since the 1960s) soil drought, which affected 16 regions of Russia and neighboring states (Kazakhstan, Kyrgyzstan, northwestern provinces of China and southeastern territories of Ukraine). The worst (for 56 years) drought in the Midwest of the United States also happened in 2012. Soil droughts are especially dangerous for strategically important agricultural regions. The Kulunda Plain, located in the steppe and forest-steppe natural zones in the south of Western Siberia, which according to the administrative-territorial division includes the steppe territories of Altai Krai, Novosibirsk (Russian Federation) and Pavlodar (Republic of Kazakhstan) oblasts, refers to such regions. For the western regions of Altai Krai, situated in the south of Western Siberia, the heat wave and drought of 2012 were unprecedented and became the most severe natural disaster in the history of the region. That drought affected more than 3 million hectares of agricultural crops. To combat it, an emergency regime was introduced.

This paper presents the findings of the comprehensive research on the development of remote microwave harbingers of droughts (Altai Krai as a case study).

2. Materials and Methods

2.1. Brief Analysis of Existing Indices and Methods

The paper [16] gives an overview of existing remote sensing methods for detecting and monitoring the areas exposed to drought. Along with traditional methods, which comprise only meteorological parameters, the combined indices based on meteorological and remote sensing data (including the indices not using ground data) are considered. Special attention is paid to the indices based on the combination of visible, near-infrared and thermal channels under day and night shooting. The advantages of applying some indices in different regions of the world are discussed. Satellite monitoring of such biophysical parameters and their anomalies such as the Soil Water Index (SWI), Normalized Difference Vegetation Index (NDVI), albedo and surface temperature provide reliable information about climatic extremes. These parameters, with the exception of soil moisture, have been regularly computed since 2000 due to satellite observations from MODIS (Medium-Resolution Imaging Spectrometer).

To detect drought and precipitation-induced waterlogging, the Satellite Climatic Extremes Index (SCEI) that is the sum of deviations from the long-term average SWI, NDVI, albedo and surface temperature normalized by the standard deviation has been developed and is used in practice [17–19]. The original approach to drought study is described in [20], where soil salinization and drought, as two major factors limiting crop yields, are considered simultaneously. It is expected that with climate change, such stresses will increase and exacerbate the risks of global food security in the future. Therefore, regular monitoring of both drought and salinity is necessary for the separation of their effects on agricultural vegetation growth. Note that different drought indices show different sensitivity to the same environmental parameters. When neglecting this fact, drought and salinization artefacts may appear. Soil salinization radically changes the dependence of brightness characteristics of soil cover on moisture [21,22].

In [23], the Nonlinear Multidimensional Drought Index (NMDI) defined through combining meteorological, hydrological and agricultural variables (precipitation, runoff and soil moisture) is presented. Duration and intensity of drought can be estimated based on NMDI. In [24], it is proposed to use the Agricultural Drought Frequency (ADFC) and Agricultural Drylands Area (ADAC) change in assessing the effects of soil drought calculated by combining the Palmer Drought Severity Index (PDSI) and the Vegetation Health Index (VHI). The results prove that ADFC and ADAC can reflect both spatial-temporal changes in characteristics of agricultural drought and the impact of ongoing drought control measures. These indices can be estimated from microwave sounding data, in particular from SMOS through calculating the areas of soil cover with different moisture content [25].

In [26], the Nonlinear Multidimensional Drought Index (NMDI) constructed by combining meteorological, hydrological and agricultural variables (precipitation, runoff and soil moisture) is discussed. The defined NMDI ensures evaluation of three characteristics of drought (duration, peak and intensity). In [27], the Combined Drought Index (CDI) was found using meteorological, ground-based and remote observations. CDI provides a synthetic and synoptic overview of drought events using a classification scheme derived from various individual indices. The paper [28] describes the recently most widely used drought indices, i.e., NMDI, VCADI, PDI, MPDI and SPDI, as well as the Soil Moisture Deficiency Index (SMDI), Evapotranspiration Deficit Index (ETDI), Evapotranspiration Fraction (EF), Vegetation Drought Temperature Index (TVDI), Vegetation Temperature Conditions Index (VTCI), Water Scarcity Index (WDI), Standard Vegetation Index (SVI) and Soil Moisture Index of Cultivated Lands (CSMI). The joint analysis of these indices provides the choice of an appropriate drought index for a particular region.

In [10], the authors report about the Multidimensional Standardized Drought Index (MSDI) developed due to a combination of the Standardized Precipitation Index (SPI) and the Standardized Soil Moisture Index (SSI) used to characterize drought. The MSDI includes meteorological and agricultural arid conditions for a general drought characteristic. In [15], it is proposed to use the Modified Reconnaissance Drought Index (mRDI) for drought analysis, taking into account both cumulative precipitation and potential evapotranspiration. This index allows to evaluate both current and historical droughts in a single metric. This index gives additional information for studying socio-economic and environmental problems of droughts; it can be applied as an effective indicator in water management and agricultural insuring.

In [29,30], a set of drought indices is used to evaluate the following drought indices: PDSI, SPI, single drought indices, vegetation and temperature conditions (TCI and MODIS), precipitation and soil moisture conditions (SMCI and AMSR-E), as well as combined drought indices, including the Integrated Microwave Drought Index (MIDI), Optimized Vegetation Drought Index (OVDI), Optimized Meteorological Drought Index (OMDI), Scaled Arid Conditions Index (SDCI) and Synthesized Drought Index (SDI). The results show that different drought indices have specific characteristics for different types of land use.

In [31], the improved Temperature-Vegetation-Soil Moisture Index (iTVMDI) was developed for drought monitoring based on remote sensing data in the optical, infrared and microwave ranges, as well as for monitoring temporal and spatial changes in drought conditions. The review article [32] discusses existing and new approaches to drought monitoring using satellite observations in the climatological and ecosystem context. In [33], a review of remote satellite sensor data in the visible and infrared ranges including the developed drought indices for detection of water stress of agricultural crops is presented. The foregoing review of scientific results obtained by various authors indicates that remote drought indices have proven their effectiveness and convenience for determining drought conditions on a regional and global scale. However, most modern drought indices are based on remote sensing data in the visible/near-infrared range, strongly influenced by clouds, water vapor content in the atmosphere and rainfall. Microwave sensors are devoid of these

disadvantages, being all-weather sensors. Meanwhile, the use of microwave vegetation drought indices in drought monitoring has not been studied in detail yet. The influence of radio frequency interference, which greatly complicates the interpretation of the results of the Earth covers' radio wave sounding in the industrial regions such as the United States, Europe and others, is less significant in agricultural regions in the south of West Siberia. Usually, radio frequency interference in the microwave range is localized in areas of large cities, and it is completely insignificant in agricultural fields where there are no active sources of microwave radiation.

In [34], an innovative drought indicator with a wider spatial and temporal coverage is proposed. It is based on the use of the brightness temperature data measured from SMOS, the so-called Standardized Brightness Temperature Index (STBI). Using the example of the 2018 drought that occurred in northern countries, it is shown that STBI provides better spatial and temporal coverage compared to other drought indices.

Various remote sensing methods for monitoring water state in vegetation are considered in [35,36]. The five most commonly used indicators of volume fraction of water in plants are the Normalized Difference Vegetation Index (NDVI) (12.2%), backscattering coefficients (10.8%), spectral reflectivity (8.1%), reflection coefficient (8.1%) and dielectric constant (8.1%). In [37], the possibilities of multisensory remote sensing for studying key phenomena and mechanisms associated with drought, including vegetation response to drought, feedback between the atmosphere and land during drought, drought-induced tree death and fires in ecosystems, recovery after drought, inherited effects, sudden drought and drought trends in the context of climate change, are studied. It is concluded that the use of multisensory remote sensing gives unique advantages for regional and global drought investigations, for instance: (1) identification of complex mechanisms of drought impact on the ecosystem components; (2) provision of continuous long-term drought-related information on a regional and global scale; (3) presentation of drought information in real time with high spatial and temporal resolution; (4) provision of evidence of drought monitoring to improve the reliability of modeling and forecasting; (5) improvement of accuracy of monitoring and assessing droughts. It is emphasized that additional drought studies focused on the use of a combination of sensors and methods (optical, microwave, hyperspectral and lidar) on various spatial and temporal scales are needed.

As shown in [38], optical depth of vegetation (VOD) obtained by microwave radiometry correlates with the total amount of water in plants. Such a correlation additionally suggests a probable relationship between VOD and the aquatic potential of woody vegetation. Accordingly, the microwave sensing data can be used in assessing the ecological state of vegetation. In [39], it is predicted that a number of drought-induced cases of tree death will increase in the future due to climate change. It is hypothesized that a relative water content (RWC) estimated by passive microwave remote sensing via VOD can be used as an empirical indicator of tree mortality.

In [40], the methods of remote microwave sensing in the optical, near-infrared and microwave ranges, as well as multispectral and hyperspectral remote sensing techniques sensitive to changes in moisture considering a type of soil and vegetation, are employed to assess droughts. The paper [41] presents the Microwave Drought Index comprising the data on precipitation, soil moisture and temperature.

In [42], the potential of using several remote sensing tools to quantify and predict drought in Northwest Africa is analyzed. Here, three additional products are considered, i.e., NDV, SWI and Land Surface Temperature (LST). The method is not a forecast; it gives a clear indication of a probable future trend of a hydrological season. The study [43] describes the Microwave Vegetation and Drought Temperature Index (MTVDI) based on the use of TVDI and brightness temperatures (T_b) measured by AMSR-E (Aqua satellite) at frequencies of 18.7 GHz, 23.8 GHz and 89.0 GHz. The developed Microwave Normalized Vegetation Difference Index (MNDVI) (AMSR-E) is also presented.

In [44], various indices are compared by the example of droughts (2011 and 2012): the Vegetation Condition Index (VCI), Temperature Conditions Index (TCI), Drought Index (PDI) and Modified PDI (MPDI) obtained on the basis of MODIS data, as well as Precipitation Condition Index (PCI), Tropical Rainfall Measuring Mission (TRMM) and the Soil Moisture Index (SMCI) obtained from AMSR-E. The following synthesized drought indices Vegetation Health Index (VHI), Vegetation Aridity Temperature Index (TVDI), Scaled Arid Conditions Index (SDCI), Integrated Microwave Drought Index (MIDI), Synthesized Drought Index (SDI), Optimized Meteorological Drought Index (OMDI) and Optimized Vegetation Drought Index (OVDI) are compared. The results suggest that different indices have strengths and weaknesses related to varying climatic conditions.

To monitor short-term drought in the Inner Mongolia region, the Integrated Microwave Drought Index calculated from TRMM and soil moisture/surface temperature data obtained from the Earth observation satellite system EOSPM Aqua is used [45,46].

The analysis of the existing drought indices clearly indicates that a reliable, highly accurate forecast of droughts remains still an unsolved scientific problem. Hence, there is a need to develop more advanced indicators and methods for monitoring droughts [47] able to operate in modern unpredictable conditions of “climate hysteria”.

2.2. Study Area

Field studies were conducted in the Kulunda Plain (an area of about 100 thousand km²) located in the steppe and forest-steppe natural zones in the south of Western Siberia (Figure 1). This strategically important agricultural region, situated in Altai Krai, Novosibirsk (Russian Federation) and Pavlodar (Republic of Kazakhstan) oblasts, is characterized by an arid climate. The amount of annual precipitation is 200–350 mm per year. The territory of the Kulunda Plain is included in the world province of soda salinization [48,49]. In some administrative districts of Altai Krai, Novosibirsk and Pavlodar oblasts, solonetz and solonetz-like complexes occupy more than 50% (and even 70–80% in some sites) of the total area of agricultural lands. The analysis of satellite data is evidence of intensification of siccation processes in the forest-steppe and steppe regions in the south of Western Siberia. A tendency towards the decrease in moisture content of the territory, the gradual increase in aridity and extreme climate, the reduction in the area of drying of highly mineralized and brackish lakes along with the expansion of the total area of salinity is noted [50,51].



Figure 1. A map of the study area with a test site (SMOS pixel).

2.3. Approach

For the regional monitoring of soil droughts, the satellite measurement data of brightness temperatures in the microwave range, the results of field measurements of physical characteristics of the underlying surface (soil temperature and moisture) and laboratory measurements of dielectric properties of soil samples from test sites were used. The bright-

ness temperature T_B on horizontal (H) and vertical (V) polarizations of the flat, slightly rough underlying surface can be calculated by the formula [52,53]

$$T_{B\ HV} = \chi_{HV} T_{ef},$$

where χ_{HV} , T_{ef} are the emissivity and effective temperature of the skin layer of the underlying surface in the layer thickness $L_{ef} = \lambda / (4\pi \sqrt{|\varepsilon|} \operatorname{tg} \delta)$, λ is the wavelength, $|\varepsilon| = \varepsilon' \sqrt{1 + \operatorname{tg}^2 \delta}$, $\operatorname{tg} \delta = \varepsilon'' / \varepsilon'$ is the tangent of loss angle and ε' , ε'' are the real and imaginary parts of complex permittivity ε of water or soil. T_{ef} is calculated as follows:

$$T_{ef} = T_0 + \int_0^\infty \frac{dT}{dz} \exp \left[- \int_0^\infty \gamma(z') dz' \right] dz,$$

where T_0 is the surface temperature, dT/dz is the local temperature gradient defined from the ground-based measurements at the test sites and

$$\gamma(z) = \frac{4\pi}{\lambda} \sqrt{\frac{\varepsilon' - \sin^2 \theta}{2} \left[\sqrt{1 + \left(\frac{\varepsilon''}{\varepsilon' - \sin^2 \theta} \right)^2} - 1 \right]}$$

is the linear coefficient of absorption capacity at incidence angle θ .

$$\chi_{HV} = 1 - r_{HV}$$

where r_H and r_V are the reflection energy coefficients for horizontal and vertical polarizations used to describe the reflective characteristics of a plane electromagnetic wave from the "free space/dielectric" interface:

$$r_H = \left| \frac{\cos \theta - \sqrt{\varepsilon - \sin^2 \theta}}{\cos \theta + \sqrt{\varepsilon - \sin^2 \theta}} \right|^2, r_V = \left| \frac{\varepsilon \cos \theta - \sqrt{\varepsilon - \sin^2 \theta}}{\varepsilon \cos \theta + \sqrt{\varepsilon - \sin^2 \theta}} \right|^2$$

2.4. Satellite Sensing Data

2.4.1. SMOS Data

L1C SMOS [54] was employed to measure the brightness temperature of the underlying surface. The product contained values of the brightness temperature obtained at an incidence angle of 42.5° on horizontal and vertical polarization. Here, we used only values of T_B on horizontal polarization. L1C data were represented as a discrete geodetic grid DGG ISEA 4H9 [55], the fragment of which is given in Figure 1. The linear cell size is 16 km and the cell area is 195 km². The L1C product is based on the data from a passive microwave 2D radiometer ($\lambda = 0.21$ cm) and its longitudinal and transverse resolutions for an incidence angle of 42.5° are 64 and 35 km, respectively. Thus, the value for any cell in the L1C product is generated by the underlying surface area of 1760 km². SMOS sensors receive radiation from some objects with different emissivity if the underlying surface is spatially inhomogeneous. The value T_B of the cell that includes Lake Kulundinskoye is formed by the lake season-dependent area, the sensed area (35–44%) and the adjacent steppe (56–65%).

2.4.2. MODIS Data

The brightness temperature of the underlying surface was estimated with the use of daily data from the infrared radiometer MODIS/Terra (product MOD11A1) available in the database LP DAAC (<https://lpdaac.usgs.gov> (accessed on 1 October 2022)). This product contained values of the surface temperature with a resolution of 1 km, an accuracy of ± 1 K and a fixed measurement time. MODIS algorithms were applied for temperature retrieval [56] based on the results of passive scanning of upwelling radiation with a wavelength of 10–12 micrometers. The time difference between MODIS and MIRAS measurements did not exceed 2 h. Resolution of radiometers MIRAS (40 km²) and MODIS (1 km²) varied significantly. The analysis of MODIS data shows minor (2 K) variations in

the underlying surface temperature within each SMOS grid cell; therefore, the resolution of the MODIS product can be lowered to the SMOS data level through data smoothing.

2.5. Meteorological Data

For the joint analysis of the satellite information and meteorological parameters of the territory, we used the dataset on soil temperature, snow cover, precipitation, air humidity and surface wind velocity from <https://rp5.ru/> (accessed on 1 October 2022). The choice of the listed meteorological parameters is due to the significant influence of these parameters on soil moisture. Snow cover, along with the moisture content of frozen soil, determines the initial moisture amount in the soil cover. The frequency and intensity of summer precipitation affect the spatial and temporal distribution of soil moisture throughout the growing season. The temperature of the surface layer of the soil and the distribution of water vapor in the surface layer of atmosphere depend on the wind speed. In turn, soil moisture, along with the granulometric composition and concentration of water-soluble mineral salts and organic substances, affects the brightness temperature T_{BH} . However, none of the meteorological parameters considered separately are sufficient to predict drought.

2.6. Field Data

The territories falling into the pixel of the MIRAS receiver (cell 4010460 of the DGG ISEA 4H9 geodetic grid) were selected as the main objects of our study, the main landscape of which was represented by plowed fields with agricultural crops. The area of water bodies did not exceed 5%, and settlements less than 1%. The area of woodlands and artificial tree plantations on light- and medium-loamy soils was insignificant. Soil density in the 0–5 cm surface layer changed from $\rho = 1.1$ to $\rho = 1.3$ g/cm³. Soil temperature in this layer varied depending on the time of day from 18–60 °C, and at a depth of 30–70 cm varied from 20 to 25 °C. Volume fraction of water in the surface layer (0–5 cm) was within 0.05–0.35 cm³/cm³.

2.7. Laboratory Measurements of Dielectric Characteristics of Soils

In order to calibrate the satellite data and to establish the experimental and theoretical dependences $\chi(W)$, the dielectric properties of samples from the test sites were measured.

The dielectric parameters of all samples were measured at a temperature of 25 ± 1 °C on the bridge-type laboratory set-up using a phase difference meter FK2-18 (Figure 2). The set-up consisted of the following main elements: G—the high-frequency signal generator G4-78 (1.16–1.78 GHz); DMS—the matched power divider; LPD—the line of variable length; A1, A2 and A3—matching coaxial attenuators; I—the measuring unit FK2-18; K—the coaxial sample container made in the form of a segment of a coaxial line.

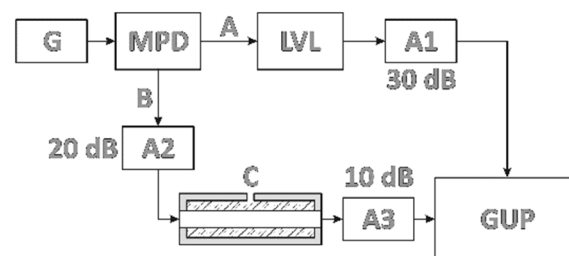


Figure 2. Block diagram of a bridge-type laboratory set-up based on the phase meter $\Phi K2-18$.

We measured attenuation (A) (dB) and phase shift ($\Delta\varphi$) (in degrees) of electromagnetic waves passing through the test sample placed in a 3.7 cm³ coaxial waveguide. The set-up had the following technical characteristics: the range of unambiguous phase and attenuation measurements made up 180 and 0–60 dB, respectively; the error of attenuation and phase measurements was 0.2 dB.

Values of the skin layer L and emissive capacity on horizontal polarization at an incidence angle of 42.5° were calculated using the results of dielectric measurements. With the increase in volume humidity of $0.06\text{--}0.45\text{ cm}^3/\text{cm}^3$, the skin layer values varied from $19\text{--}4\text{ cm}$.

To describe quantitatively the water in the samples, we used volumetric ($W = V_W/V$ [cm^3/cm^3]) and mass ($W_M = M_W/M$ [g/g]) fractions interrelated as the ratio $W = (\rho/\rho_W)W_M$, where V, V_W —the volumes of a sample and a liquid phase and $M = M_{\text{dry}} + M_W, M_{\text{dry}}, M_W, \rho, \rho_{\text{dry}}, \rho_W = 1$ —the mass and density of wet samples, dry samples and water. To define V_W , the samples were weighed by an analytical balance with an accuracy of 0.001 g , then placed in an oven, dried to a constant mass at a temperature of 105°C and reweighed.

The dielectric properties of soil were measured at a gradual drying of W ($0.45\text{--}0.006\text{ cm}^3/\text{cm}^3$). Before measuring, each sample was grinded and thoroughly mixed until the unified condition was reached. Depending on W and packing density in the measuring container, the mass of the study samples made up $7\text{--}10\text{ g}$, $\rho_{\text{wet}} = 1.2 \div 1.4\text{ g/cm}^3$ and $\rho_{\text{dry}} = 1.1 \div 1.3\text{ g/cm}^3$.

3. Results

3.1. Dependence of $\chi(W)$

Based on the results of laboratory measurements of dielectric characteristics of soils from the test site, the dependence $\chi(W)$ (Figure 3) approximated by straight lines with a break point with $W_t = 0.12$ was calculated as

$$\chi = \begin{cases} A - B \cdot W, & 0 \leq W \leq 0.12, \\ C - D \cdot W + E \cdot W^2, & 0.12 \leq W \leq 0.40, \end{cases} \quad (1)$$

where empirical coefficients A, B, C, D, E are shown in Table 1.

Table 1. Empirical coefficients in Formula (1).

Polarization	A	B	R ²	σ	C	D	E	R ²	σ
Nadir	0.98594	1.09117	−0.995	0.0097	1.02285	1.3898	0.54841	0.991	0.0096
Vertical	1.0254	0.5485	−0.98	0.0096	1.07701	0.976	0.80791	0.971	0.0087
Horizontal	0.88358	1.43197	−0.998	0.0087	0.90949	1.73483	0.73615	0.985	0.015

R^2 is the coefficient of determination, σ is the standard deviation.

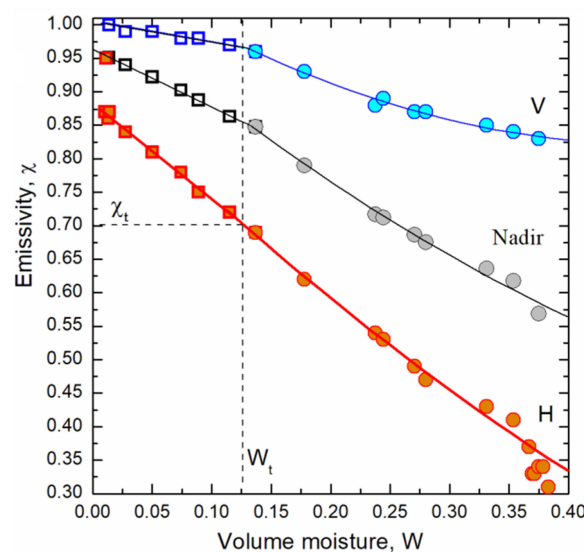


Figure 3. Dependence of emissivity (χ) on volume fraction of water in soil (W).

3.2. Long-Term Seasonal Dynamics of Brightness Temperatures for the Test Site

The long-term seasonal variations in emissivity of the underlying surface carry the objective information about the ongoing hydrological and climatic changes, including phenological shifts. For example, Figure 4 shows the long-term seasonal dynamics of brightness (1) and physical (2) temperatures of the underlying surface of the test area. The calculated dependences $T(D)$ and $T_{BH}(D)$ have the form

$$T_{BH} = -1963.01724 + 8.93389 \times 10^{-4} \times D, \sigma = 0.002,$$

$$T = 1577.96072 - 5.25445 \times 10^{-4} \times D, \sigma = 0.001,$$

where D is the Julian day number.

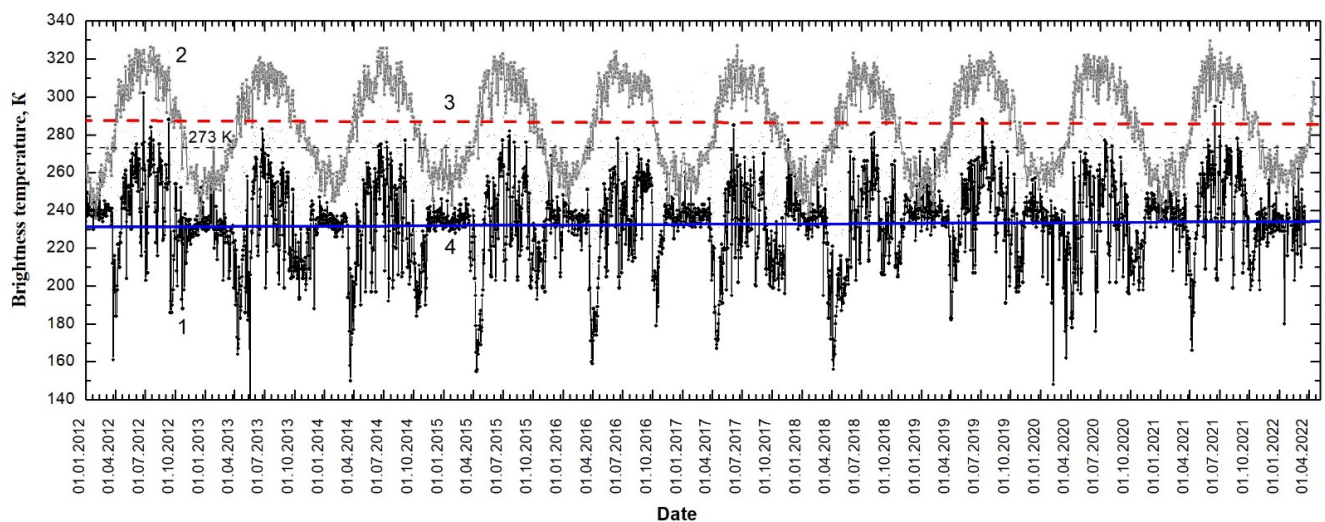


Figure 4. Dynamics of radio brightness and physical temperatures of the underlying surface in pixel 4,010,460 discrete geodetic grid DGG ISEA 4H9: 1— T_{BH} ; 2— T ; 3— $T(D)$; 4— $T_{BH}(D)$.

As seen from the above ratios, T decreased by 1.86 K, whereas T_B increased by 3.68 K over 10 years. According to (1)–(5), T_{BH} depends on T and χ [53], while χ depends on the volume fraction and phase composition of soil moisture (free, bound and crystallization water), which in turn depends on the granulometric composition of soil, mass fractions, and types of mineral salts, chemical compounds and mineral fertilizers, which change dielectric characteristics when interacting with soil moisture.

3.3. Spatial and Temporal Patterns of Brightness Temperature Distribution in the South of Western Siberia

Figure 5 depicts map schemes of spatial distribution of T_{BH} covering the drought period from June–July of 2012. The choice of this period is due to the fact that weather conditions characteristic of drought began to appear in June, peaked at the end of July and affected more than 3 million hectares of crops. On 26 July 2012, a state of emergency was introduced in the Altai Region. The SMOS data analysis was performed during all this time in order to discover the radio-physical harbingers of drought. Soil plots with high T_{BH} corresponding to low W are shown.

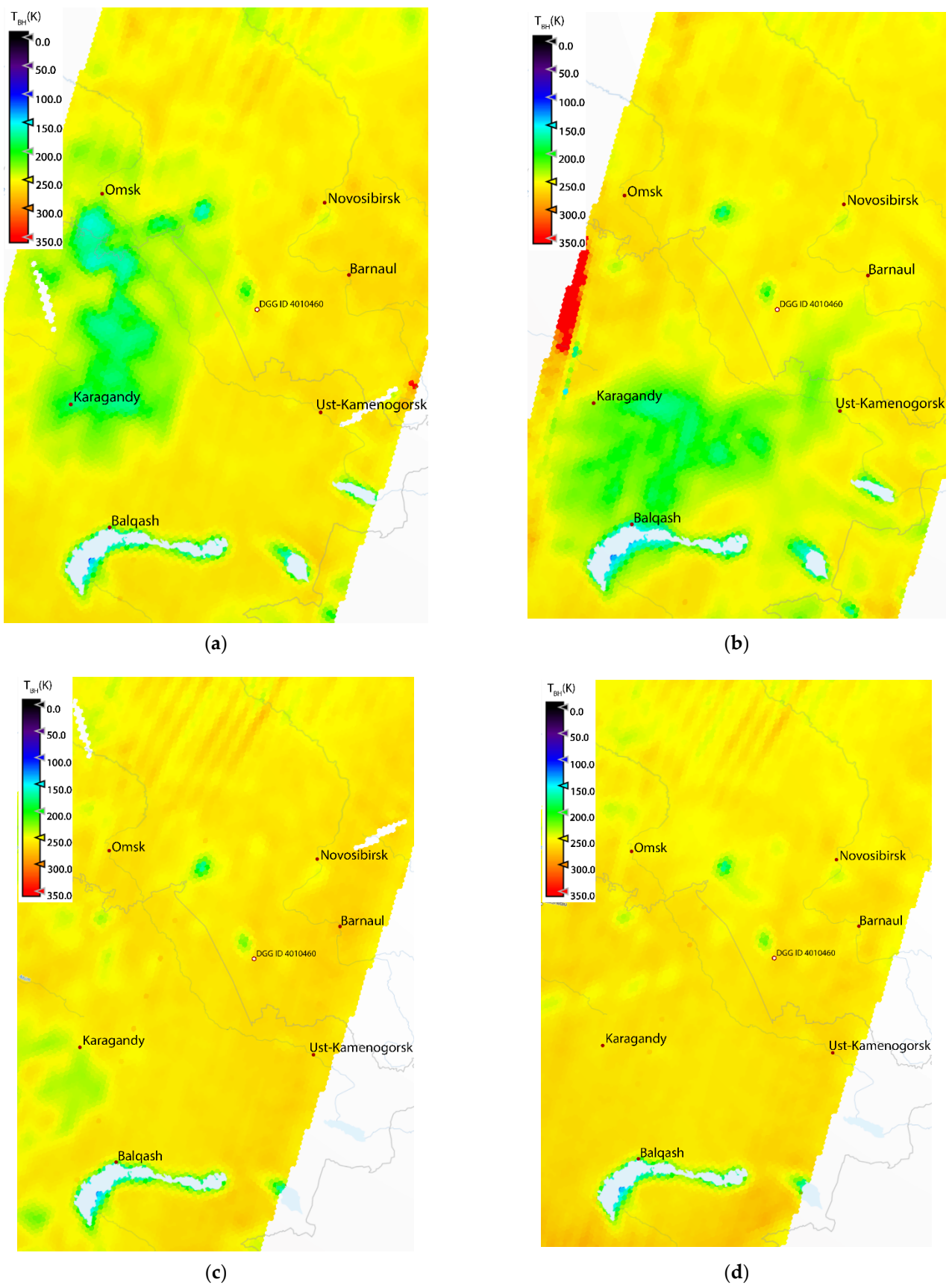


Figure 5. Map schemes of spatial distribution of brightness temperatures: (a)—10 June 2012; (b)—11 July 2012; (c)—10 June 2012; (d)—11 July 2012.

3.4. Assessing Meteorological Parameters' Effect on Brightness Temperatures of Soil Cover

The studied meteorological parameters were represented by solid (snow) and liquid (rain) precipitation, including wind velocity. Figure 6a shows the long-term seasonal changes in snow thickness (2012–2022). It can be seen that in autumn–winter, preceding summer soil droughts (2012, 2018), snow thickness did not exceed 20 cm; some sites did not see snow at all. In 2014 and 2016, this indicator in the absence of soil drought was 20–30 cm and reached 50 cm in the dry year 2020. Therefore, snow accumulation in winter is an important but not a crucial factor for breaking soil drought in summer. Intensive snowmelt causes soil moistening, which in turn leads to T_B drop.

Figure 6b shows seasonal dynamics of T_{BH} (1), T (2) and precipitation (3) for the year 2012. Free from rainfall periods are indicated by the number four and the declared emergency by the number five. Rainfalls clearly increased soil moisture and decreased T_{BH} . The amount of precipitation per day was approximately 0 mm during the periods of droughts. In other periods (from March to October), daily values vary from 0 to 19 mm, averaging 0.93 ± 0.17 mm. If we consider only the periods when precipitation is observed, then their daily values vary from 0.2 to 19 mm, averaging 3.07 ± 0.45 mm.

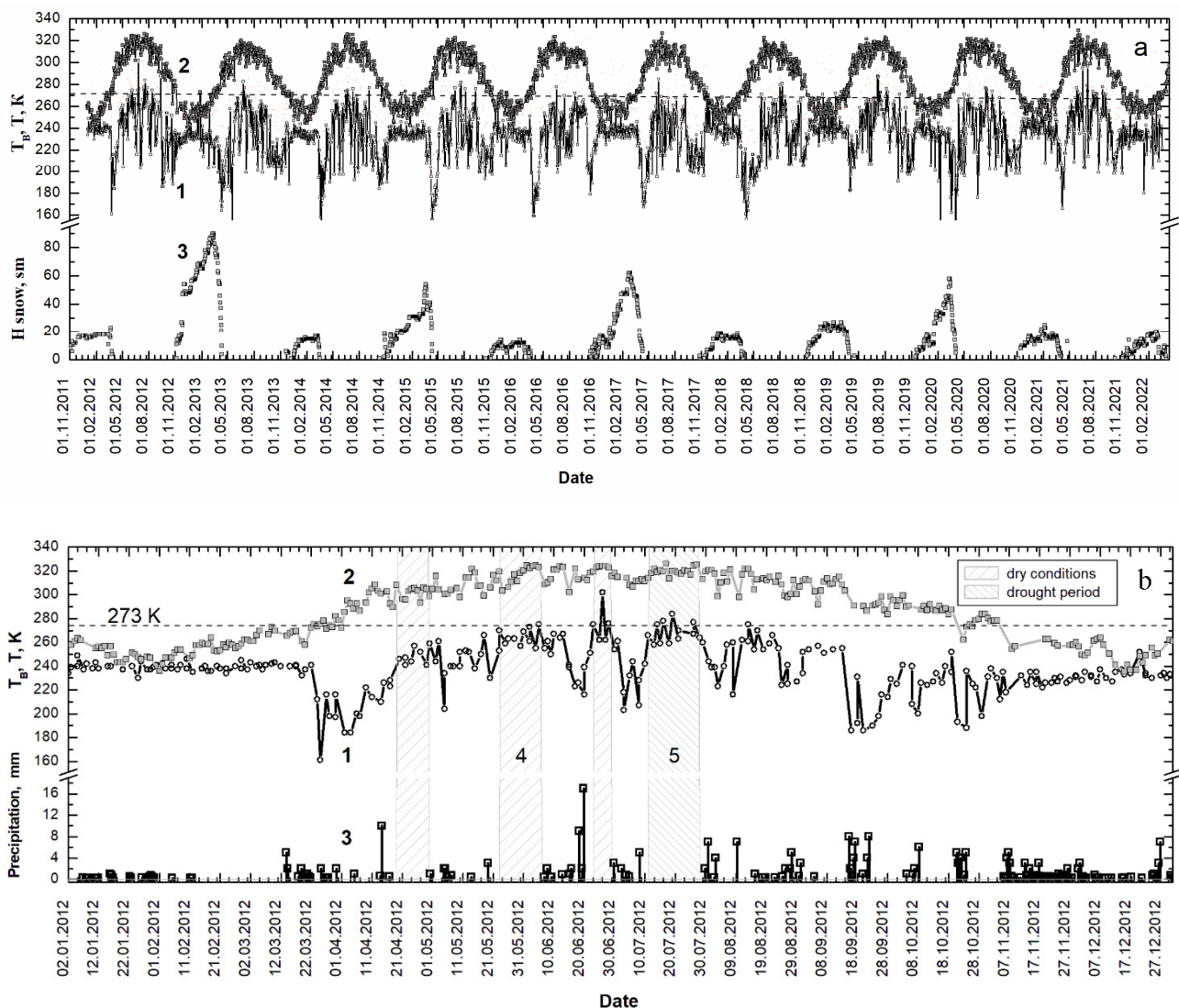


Figure 6. Cont.

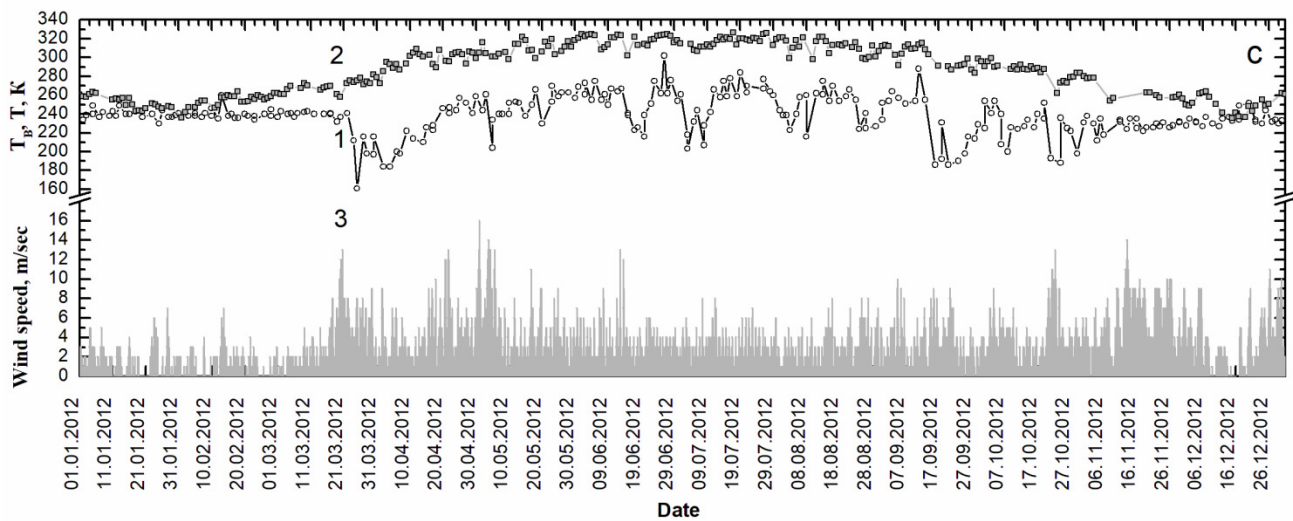


Figure 6. Seasonal dynamics of T_{BH} , T and meteorological parameters: (a) snow cover, (b) rainfall, (c) wind velocity, 1—brightness temperature T_{BH} , 2—temperature T , 3—meteorological parameters (H_{snow} in (a), Precipitation in (b), and Wind speed in (c)), 4—periods without precipitation, 5—period of drought which ended with the declaration of a state of emergency.

Figure 6c shows seasonal dynamics of T_{BH} (1), T (2) and wind velocity (3) in 2012. Average daily wind speeds (at a height of 10 m) during drought periods vary from 1.63 to 7.13 m/s, amounting to on average 3.15 ± 0.17 m/s, and in other periods (from March to October) they vary from 0.13 to 10.63 m/s, averaging 3.18 ± 0.12 m/s. A strong wind (>10 m/s) preceded a decrease in T_{BH} and T that could be due to cooling of the underlying surface. The distribution of days by wind speed is shown in Figure 7.

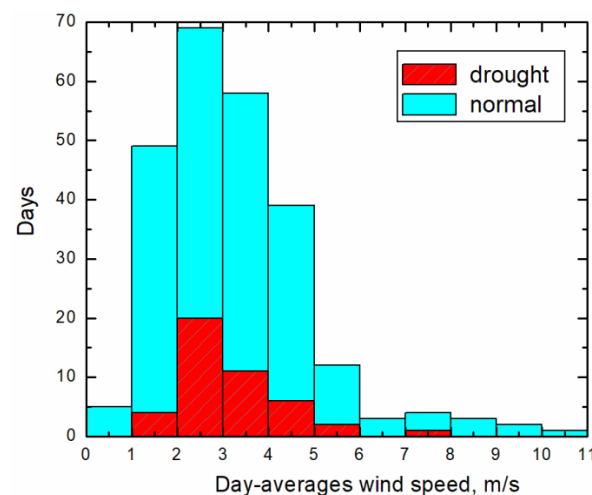


Figure 7. Distribution of days by wind speed.

4. Discussion

The experimental data analysis points to the parameters changing the moisture content of soil as major meteorological ones, which have a noticeable effect on T_{BH} . Therefore, it is important to establish W dependencies of emissivity of soil cover. The influence of T_{BH} on W has been studied since the mid-1960s [57–61]. When modeling the dielectric and radio-emitting characteristics of soils, many authors have expressed the idea of the need to quantify the influence of bound water, the volume fraction of which depends on the granulometric composition [60,62,63]. To date, a large number of studies of dielectric and radio-emitting characteristics of the Earth's covers in the microwave range have been summarized in a number of monographs and reviews [64–70].

The results of laboratory measurements of dielectric characteristics were used for calculation of dependence $W(\chi_H)$ (Figure 3):

$$W = \begin{cases} 0.60636 - 0.67946 \cdot \chi_H, R^2 = -0.99, \sigma = 0.011, 0.30 \leq \chi_H \leq 0.69, \\ 0.51668 - 0.56926 \cdot \chi_H, R^2 = -0.95, \sigma = 0.015, 0.69 \leq \chi_H \leq 0.92, \end{cases}$$

Figure 8 shows the seasonal dynamics of T_{BH} (1), T (2) and W (3) in 2012 for the test area. The value of W was calculated on the basis of satellite measurements of T_{BH} and ground-based measurements of T according to Formula (1).

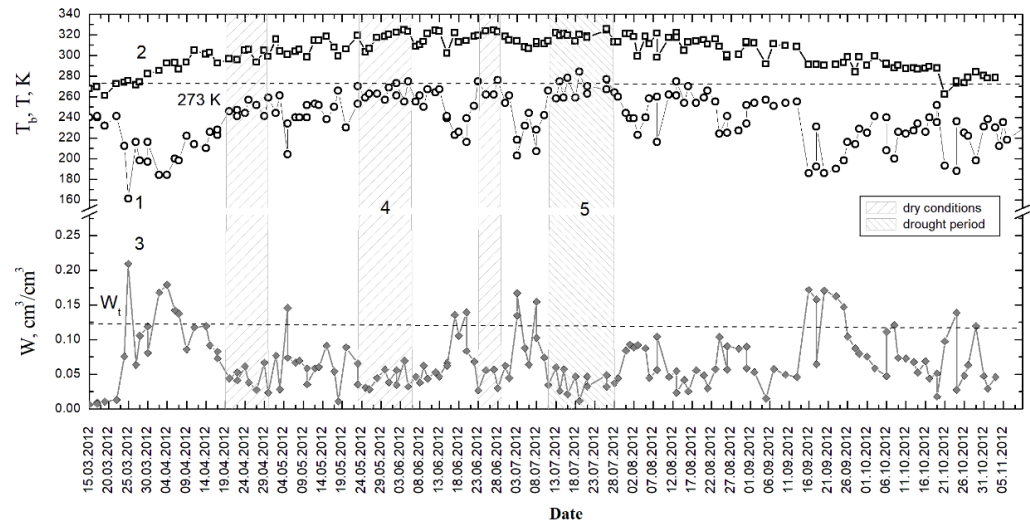


Figure 8. Seasonal dynamics of T_{BH} , T and W , 1—brightness temperature T_{BH} , 2—temperature T , 3—volume fraction of water in soil W ; 4—periods of drought, 5—period of drought which ended with the declaration of a state of emergency.

The graphs demonstrate that $W < 0.13 \text{ cm}^3/\text{cm}^3$ is observed mostly during a warm season. This value is comparable to the maximum volume fraction of bound water (W_i) in soil, inaccessible to plants. Low values of W are associated with insignificant snow reserves that accumulated during the winter of 2011/2012 and insufficient rainfalls. Since the beginning of the year, there was about 60 mm of precipitation, whereas during the two weeks preceding the introduction of the emergency regime (26 July 2012) there was no precipitation at all. Moistened by rainfalls, soil was soaked to a 3–5 cm depth and dried out within 2–3 days, showing extremely low values of W . Insiccation rates $\Delta W/\Delta D$ varied from 0.01 to 0.09 cm^3/cm^3 per day. The corresponding increase rates of dT_{BH}/dD ranged from 3.5–17 K/day. It was found that a rise in T_{BH} by 3.5 K corresponded to drop of W by 0.01 cm^3/cm^3 . The dependence of dT_{BH}/dD on dW/dD has the form

$$dT_{BH}/dD = 0.06944 + 249.54619 \cdot dW/dD, R^2 = 0.95, \sigma = 2.4.$$

Using satellite measurements of T_{BH} and dependence $W(\chi)$, we constructed maps schemes of the spatial distribution of W (Figure 9).

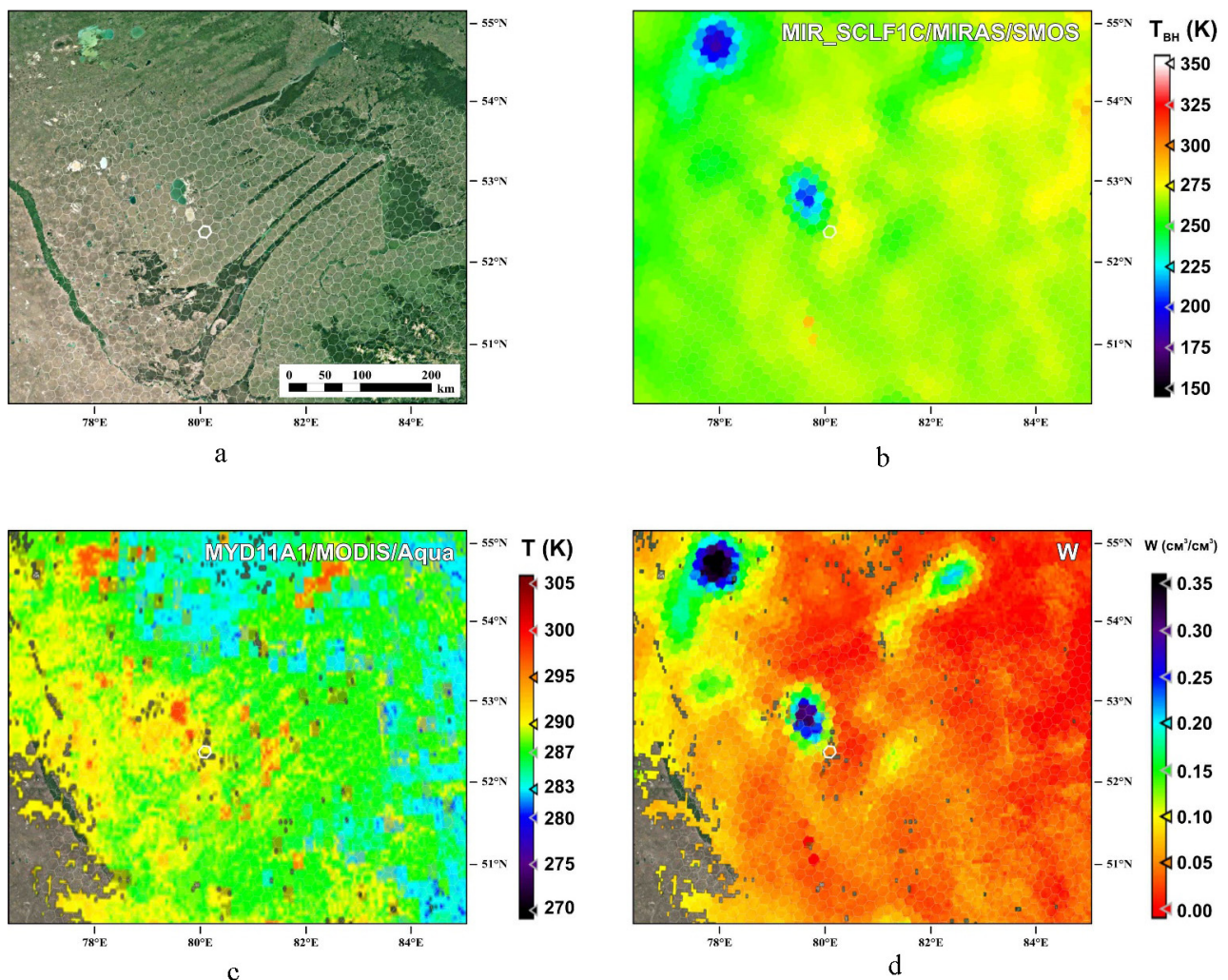


Figure 9. Map schemes of terrain (a) and spatial distribution of T_{BH} (b), T (c) and W (d).

5. Conclusions

The comprehensive analysis of remote, field and laboratory data suggests that the rate of change in the brightness temperature (dT_{BH}/dD) characterizing the rate of fall of volume humidity of soil can be used as a radio-physical harbinger of drought.

It appeared from the example of the drought of 2012 occurring in Altai Krai, the strongest one since the 1960s, that daily changes in dT_{BH}/dD reached 17 K/day. This corresponded to a change in W by $0.009 \text{ cm}^3/\text{cm}^3$ per day. For example, $W_t = 0.13 \text{ cm}^3/\text{cm}^3$ results in soil drying out. For instance, highly moistened soil at $W = 0.40 \text{ cm}^3/\text{cm}^3$ (field moisture capacity) loses its moisture in 3 days.

Map schemes of spatial distribution of $W(T_{BH}/T)$ constructed with the use of the data on remote measurements of T_{BH} in the microwave range, T in the infrared range and laboratory dependence $W(\chi_H)$ allow to identify the areas of intense drought and to assess the extent of drought.

The long-term dynamics of T_{BH} (JD) and T (JD) in some sites make it possible to identify trends of changes in T_{BH} and T with their further application in prediction of scenarios of climate change.

Author Contributions: Conceptualization, A.R.; methodology, A.R., I.R., I.K. and D.T.; software, I.R. and I.K.; validation, I.R., I.K., D.T. and D.R.; formal analysis, I.R., I.K., D.T. and D.R.; investigation, A.R., I.R., I.K., D.T. and D.R.; resources, A.R., I.K. and D.T.; data curation, I.R., I.K., D.T. and D.R.; writing—original draft preparation, A.R., I.R. and I.K.; writing—review and editing, A.R., I.R., I.K., D.T. and D.R.; visualization, I.R., I.K. and D.R.; supervision, A.R.; project administration, A.R.; funding acquisition, A.R. All authors have read and agreed to the published version of the manuscript.

Funding: This research was funded by the Russian Science Foundation Grant No. 22-17-20041, <https://rscf.ru/project/22-17-20041/> (accessed on 1 October 2022).

Data Availability Statement: Not applicable.

Conflicts of Interest: The authors declare no conflict of interest.

References

1. European Commission; Joint Research Centre. *World Atlas of Desertification: Rethinking Land Degradation and Sustainable Land Management*; Hill, J., Von Maltitz, G., Sommer, S., Reynolds, J., Hutchinson, C., Cherlet, M., Eds.; Publications Office: Luxembourg, 2018. [CrossRef]
2. Tarpley, J.D.; Schneider, S.R.; Money, R.L. Global vegetation indices from the NOAA-7 meteorological satellite. *J. Clim. Appl. Meteorol.* **1984**, *23*, 491–494. [CrossRef]
3. Kogan, F.N. Droughts of the late 1980s in the United States as derived from NOAA polarorbiting satellite data. *Bull. Am. Meteorol. Soc.* **1995**, *76*, 655–668. [CrossRef]
4. Clapp, J. The Global Food Crisis: Governance Challenges and Opportunities. 270 p. January 2009. Available online: https://www.cigionline.org/sites/default/files/the_global_food_crisis.pdf (accessed on 1 October 2022).
5. FAO; IFAD; UNICEF; WFP; WHO. *The State of Food Security and Nutrition in the World. Repurposing Food and Agricultural Policies to Make Healthy Diets More Affordable*; FAO: Rome, Italy, 2022. [CrossRef]
6. Headey, D.D. The Impact of the Global Food Crisis on Self-Assessed Food Security. *World Bank Econ. Rev.* **2013**, *27*, 1–27. Available online: <http://www.jstor.org/stable/43774096> (accessed on 1 October 2022). [CrossRef]
7. Chandrasekar, K.; Sesha Sai, M.V.R.; Roy, P.S.; Dwevedi, R.S. Land Surface Water index (LSWI) response to rainfall and NDVI using the MODIS vegetation index product. *Int. J. Remote Sens.* **2010**, *31*, 3987–4005. [CrossRef]
8. Gao, B.C. NDWI—A Normalized Difference Water Index for remote sensing of vegetation liquid water from space. *Remote Sens. Environ.* **1996**, *58*, 257–266. [CrossRef]
9. World Meteorological Organization (WMO); Global Water Partnership (GWP). *Handbook of Drought Indicators and Indices*; Svoboda, M., Fuchs, B.A., Eds.; Integrated Drought Management Tools and Guidelines Series 2; Integrated Drought Management Programme (IDMP): Geneva, Switzerland, 2016; 45p.
10. Hao, Z.; Kouchak, A.A. Multivariate Standardized Drought Index: A multi-index parametric approach for drought analysis. *Adv. Water Resour.* **2013**, *57*, 12–18. [CrossRef]
11. Vicente-Serrano, S.M.; Begueria, S.; Lopez-Moreno, J.I. A multi-scalar drought index sensitive to global warming: The Standardized Precipitation Evapotranspiration Index. *J. Clim.* **2010**, *23*, 1696–1718. [CrossRef]
12. Woli, P.; Jones, J.W.; Ingram, K.T.; Fraisse, C.W. Agricultural Reference Index for Drought (ARID). *Agron. J.* **2012**, *104*, 287–300. [CrossRef]
13. Zargar, A.; Sadiq, R.; Naser, B.; Khan, F.I. A review of drought indices. *Environ. Rev.* **2011**, *19*, 333–349. [CrossRef]
14. Kchouk, S.; Melsen, L.; Walker, D.; van Oel, P. A review of drought indices: Predominance of drivers over impacts and the importance of local context. *Nat. Hazards Earth Syst. Sci. Discuss.* **2021**, 1–28. [CrossRef]
15. Yilmaz, B. Proposed index for drought assessment: Modified reconnaissance drought index (mRDI). *J. Environ. Prot. Ecol.* **2018**, *19*, 1796–1804.
16. Shcherbenko, E.V. Remote methods for detecting agricultural drought. *Mod. Probl. Remote Sens. Earth Space* **2007**, *4*, 408–419. (In Russian)
17. Zolotokrylin, A.N.; Titkova, T.B.; Cherenkova, E.A.; Vinogradova, V.V. Comparative study of droughts 2010 and 2012 in the European Russia from meteorological and MODIS data. *Mod. Probl. Remote Sens. Earth Space* **2013**, *10*, 246–253. (In Russian)
18. Zolotokrylin, A.N.; Titkova, T.B. Satellite climatic extremes index of dryland. *Arid. Ecosyst.* **2012**, *4*, 203–208. [CrossRef]
19. Zolotokrylin, A.N.; Titkova, T.B.; Cherenkova, E.A.; Vinogradova, V.V. Satellite index for assessing climatic extremes in arid lands (on the example of the Kuma-Manych depression). *Mod. Probl. Remote Sens. Earth Space* **2012**, *9*, 114–121. (In Russian)
20. Wen, W.; Timmermans, J.; Chen, Q.; Bodegom, P. M A Review of Remote Sensing Challenges for Food Security with Respect to Salinity and Drought Threats. *Remote Sens.* **2021**, *13*, 6. [CrossRef]
21. Mukherjee, S.; Mishra, A.; Trenberth, K.E. Climate change and drought: A perspective on drought indices. *Curr. Clim. Change Rep.* **2018**, *4*, 145–163. [CrossRef]
22. Romanov, A.N. Dielectric Behavior of Sodic Solonchak at 1.41 GHz in the South of Western Siberia. *IEEE Trans. Geosci. Remote Sens.* **2019**, *57*, 9517–9523. [CrossRef]
23. Yang, J.; Chang, J.; Wang, Y.; Yao, J. Comprehensive drought characteristics analysis based on a nonlinear multivariate drought index. *J. Hydrol.* **2017**, *557*, 651–667. [CrossRef]

24. Wu, B.; Ma, Z.; Yan, N. Agricultural drought mitigating indices derived from the changes in drought characteristics. *Remote Sens. Environ.* **2020**, *244*, 111813. [[CrossRef](#)]
25. Romanov, A.N.; Khvostov, I.V. Microwave remote monitoring of Altai catastrophic flood dynamics using SMOS data. *IEEE Geosci. Remote Sens. Lett.* **2015**, *12*, 2036–2040. [[CrossRef](#)]
26. Aladaileh, H.; Al Qinna, M.; Karoly, B.; Al-Karablieh, E.; Al Bakri, J.; Rakonczai, J. Applicability of a combined drought index to monitoring drought in Jordan. *J. Eng. Res. Appl.* **2019**, *9*, 20–39.
27. Chattopadhyay, N.; Malathi, K.; Tidke, N.; Attri, S.D.; Ray, K. Monitoring agricultural drought using combined drought index in India. *J. Earth Syst. Sci.* **2020**, *129*, 155. [[CrossRef](#)]
28. Zhang, H.W.; Chen, H.L. The Review of Drought Index in Advance. In Proceedings of the International Conference on Ecological Protection of Lakes-Wetlands-Watershed and Application of 3S Technology (EPLWW3S 2011), Nanchang, China, 25–26 June 2011; Volume 2, pp. 533–537.
29. Wei, W.; Zhang, J.; Zhou, L.; Xie, B.; Zhou, J.; Li, C. Comparative evaluation of drought indices for monitoring drought based on remote sensing data. *Environ. Sci. Pollut. Res.* **2021**, *28*, 20408–20425. [[CrossRef](#)] [[PubMed](#)]
30. Li, Z.; Han, Y.; Hao, T. Assessing the Consistency of Remotely Sensed Multiple Drought Indices for Monitoring Drought Phenomena in Continental China. *IEEE Trans. Geosci. Remote Sens.* **2020**, *58*, 5490–5502. [[CrossRef](#)]
31. Wang, Z.D.; Guo, P.; Wan, H. Improved drought monitoring method based on multisource remote sensing data. In Proceedings of the IEEE International Geoscience and Remote Sensing Symposium (IGARSS), Virtual, 26 September–2 October 2020; pp. 5282–5285.
32. Kouchak, A.; Farahmand, A.; Melton, F.S.; Teixeira, J.; Anderson, M.C.; Wardlow, B.D.; Hain, C.R. Remote sensing of drought: Progress, challenges and opportunities. *Rev. Geophys.* **2015**, *53*, 452–480. [[CrossRef](#)]
33. Gerhards, M.; Schlerf, M.; Rascher, U.; Udelhoven, T.; Juszczak, R.; Alberti, G.; Miglietta, F.; Inoue, Y. Analysis of Airborne Optical and Thermal Imagery for Detection of Water Stress Symptoms. *Remote Sens.* **2018**, *10*, 1139. [[CrossRef](#)]
34. Gerhards, M.; Schlerf, M.; Mallick, K.; Udelhoven, T. Challenges and Future Perspectives of Multi-/Hyperspectral Thermal Infrared Remote Sensing for Crop Water-Stress Detection: A Review. *Remote Sens.* **2019**, *11*, 1240. [[CrossRef](#)]
35. Quemada, C.; Pérez-Escudero, J.M.; Gonzalo, R.; Ederra, I.; Santesteban, L.G.; Torres, N.; Iriarte, J.C. Remote Sensing for Plant Water Content Monitoring: A Review. *Remote Sens.* **2021**, *13*, 2088. [[CrossRef](#)]
36. Ma, S.; Zhou, Y.; Gowda, P.H.; Dong, J.; Zhang, G.; Kakani, V.G.; Wagle, P.; Chen, L.; Flynn, K.C.; Jiang, W. Application of the water-related spectral reflectance indices: A review. *Ecol. Indic.* **2018**, *98*, 68–79. [[CrossRef](#)]
37. Jiao, W.; Wang, L.; McCabe, M.F. Multi-sensor remote sensing for drought characterization: Current status, opportunities and a roadmap for the future. *Remote Sens. Environ.* **2021**, *256*, 112313. [[CrossRef](#)]
38. Holtzman, N.M.; Anderegg, L.D.; Kraatz, S.; Mavrovic, A.; Sonnentag, O.; Pappas, C.; Cosh, M.H.; Langlois, A.; Lakhankar, T.; Tesser, D.; et al. L-band vegetation optical depth as an indicator of plant water potential in a temperate deciduous forest stand. *Biogeosciences* **2021**, *18*, 739–753. [[CrossRef](#)]
39. Rao, K.; Anderegg, W.R.; Sala, A.; Martínez-Vilalta, J.; Konings, A.G. Satellite-based vegetation optical depth as an indicator of drought-driven tree mortality. *Remote Sens. Environ.* **2019**, *227*, 125–136. [[CrossRef](#)]
40. Yuan, Y.; Xi, C.; Jing, Q. Advance in Agricultural Drought Monitoring Using Remote Sensing Data. *Spectrosc. Spectr. Anal.* **2019**, *39*, 1005–1012.
41. Zhang, A.Z.; Jia, G.S.; Wang, H.S. Improving meteorological drought monitoring capability over tropical and subtropical water-limited ecosystems: Evaluation and ensemble of the Microwave Integrated Drought Index. *Environ. Res. Lett.* **2019**, *14*, 044025. [[CrossRef](#)]
42. Le Page, M.; Zribi, M. Analysis and Predictability of Drought in Northwest Africa Using Optical and Microwave Satellite Remote Sensing Products. *Sci. Rep.* **2019**, *9*, 1466. [[CrossRef](#)]
43. Liu, L.; Liao, J.; Chen, X.; Zhou, G.; Su, Y.; Xiang, Z.; Wang, Z.; Liu, X.; Li, Y.; Wu, J.; et al. The Microwave Temperature Vegetation Drought Index (MTVDI) based on AMSR-E brightness temperatures for long-term drought assessment across China (2003–2010). *Remote Sens. Environ.* **2017**, *199*, 302–320. [[CrossRef](#)]
44. Zhang, L.; Jiao, W.; Zhang, H.; Huang, C.; Tong, Q. Studying drought phenomena in the Continental United States in 2011 and 2012 using various drought indices. *Remote Sens. Environ.* **2017**, *190*, 96–106. [[CrossRef](#)]
45. Miao, T.; Zhiming, W.; Kun, Y.; Jingjing, W. Study on the Precipitation Temperature Index and its application in drought and flood disasters. In Proceedings of the 6th International Conference on Agro-Geoinformatics, Fairfax, VA, USA, 7–10 August 2017; pp. 290–293.
46. Shen, Z.; Zhang, Q.; Singh, V.; Peng, S.; Song, C.; Yu, H. Agricultural drought monitoring across Inner Mongolia, China: Model development, spatiotemporal patterns and impacts. *J. Hydrol.* **2019**, *571*. [[CrossRef](#)]
47. Yihdego, Y.; Vaheddoost, B.; Al-Weshah, R.A. Drought indices and indicators revisited. *Arab. J. Geosci.* **2019**, *12*, 69. [[CrossRef](#)]
48. Bazilevich, N.I. *Geochemistry of Soils with Soda Salinity*; Nauka: Moscow, Russia, 1965; 349p. (In Russian)
49. Kovda, V.A. *Problems of Combating Desertification and Salinization of Irrigated Soils*; Kolos: Moscow, Russia, 1984; 304p. (In Russian)
50. Glushkova, N.V.; Chupina, D.A.; Pchel'nikov, D.V.; Boldyrev, I.I.; Selyatitskaya, N.A. Mapping and monitoring of aridization processes in the south of the West Siberian plain. *Geogr. Nat. Resour.* **2016**, *1*, 133–140. (In Russian)
51. Anopchenko, L.Y.; Yakutin, M.V. Aridization of the climate in the south of Western Siberia and soil salinization. *Interexpo Geo-Sib.* **2012**, *2*, 207–211. (In Russian)

52. Njoku, E.G.; Kong, J.A. Theory for passive microwave remote sensing of near-surface soil moisture. *J. Geophys. Res.* **1977**, *82*, 3108–3118. [[CrossRef](#)]
53. Sharkov, E.A. *Passive Microwave Remote Sensing of the Earth: Physical Foundations*; Springer: Berlin, Germany, 2003.
54. Gutierrez, A.; Castro, R.; Vieira, P.; Lopes, G.; Barbosa, J. SMOS L1 Processor L1c Data Processing Model. SO-DS-DME-L1OP-0009. No. 2.17. 2017. Available online: <https://earth.esa.int/eogateway/documents/20142/37627/SMOS-L1c-Data-Processing-Models.pdf> (accessed on 1 October 2022).
55. Sahr, K.; White, D.; Kimerling, A.J. Geodesic Discrete Global Grid Systems. *Cartogr. Geogr. Inf. Sci.* **2003**, *30*, 121–134. [[CrossRef](#)]
56. Wan, Z. *MODIS Land-Surface Temperature Algorithm Theoretical Background Document (LST ATBD)*; Institute for Computational Earth System Science, University of California: Santa Barbara, CA, USA, 1999. Available online: https://modis.gsfc.nasa.gov/data/atbd/atbd_mod11.pdf (accessed on 1 October 2022).
57. Basharinov, A.E.; Tuchkov, L.T.; Polyakov, V.S.; Ananov, N.I. *Measurement of Radiothermal and Plasma Microwave Radiation*; Soviet Edition: Moscow, Russia, 1968; 390p. (In Russian)
58. Basharinov, A.E.; Gurchich, A.S.; Egorov, S.T. *Radiothermal Radiation of the Earth as a Planet*; Nauka: Moscow, Russia, 1974; 188p. (In Russian)
59. Schmugge, T.J.; Gloersen, P.W.; Wilheit, T.; Geiger, F. Remote Sensing of Soil Moisture with Microwave Radiometry. *J. Geophys. Res.* **1974**, *79*, 317–323. [[CrossRef](#)]
60. Jackson, T.J.; Schmugge, T.J. Passive Microwave Remote Sensing System for Soil Moisture: Some Supporting Research. *IEEE Trans. Geosci. Remote Sens.* **1989**, *27*, 225–235. [[CrossRef](#)]
61. Ulaby, F.T. Passive Microwave Remote Sensing of the Earth's Surface. *IEEE Trans. Antennas Propag.* **1976**, *24*, 112–115. [[CrossRef](#)]
62. Schmugge, T.J. Effect of Texture on Microwave Emission from Soils. *IEEE Trans. Geosci. Remote Sens.* **1980**, *GE-18*, 353–361. [[CrossRef](#)]
63. Komarov, S.A.; Mironov, V.L.; Romanov, A.N.; Rychkova, N.V. Remote determination of moisture content of soil in the Altai Krai. *Eurasian Soil Sci.* **1993**, *25*, 39–44.
64. Ulaby, F.T.; Moore, R.K.; Fung, A.K. *Microwave Remote Sensing: Active and Passive: Volume 3—From Theory to Applications*; Artech House Inc.: Norwood, MA, USA, 1986; pp. 1065–2162. ISBN 0890061920. [[CrossRef](#)]
65. Wang, J.R.; Schmugge, T.J. An Empirical Model for the Complex Dielectric Permittivity of Soils as a Function of Water Content. *IEEE Trans. Geosci. Remote Sens.* **1980**, *GE-18*, 288–295. [[CrossRef](#)]
66. Njoku, E.G.; Entekhabi, D. Passive microwave remote sensing of soil moisture. *J. Hydrol.* **1996**, *184*, 101–129. [[CrossRef](#)]
67. Ho, P.P. (Ed.) *Geoscience and Remote Sensing*; IntechOpen: London, UK, 2009; Available online: <https://www.intechopen.com/books/3345> (accessed on 1 October 2022).
68. Lakhankar, T.; Krakauer, N.; Khanbilvardi, R. Applications of microwave remote sensing of soil moisture for agricultural applications. *Int. J. Terraspace Sci. Eng.* **2009**, *2*, 81–91.
69. Nghiem, S.V.; Wardlow, B.D.; Allured, D.; Svoboda, M.; LeComte, D.; Rosencrans, M.; Chan, S.K.; Neumann, G. *Microwave Remote Sensing of Soil Moisture Science and Applications*; Drought Mitigation Center Faculty Publications: Lincoln, NE, USA, 2012; p. 104. Available online: <http://digitalcommons.unl.edu/droughtfacpub/104> (accessed on 1 October 2022).
70. Jackson, T.J. Passive Microwave Remote Sensing of Soil Moisture and Regional Drought Monitoring. In *Monitoring and Predicting Agricultural Drought: A Global Study*; Oxford Academic: New York, NY, USA, 2005. [[CrossRef](#)]